Symmetry-forbidden intervalley scattering by atomic defects in monolayer transition-metal dichalcogenides

Kaasbjerg, Kristen; Martiny, Johannes H. J.; Low, Tony; Jauho, Antti-Pekka

Published in:
Physical Review B (Condensed Matter and Materials Physics)

Link to article, DOI:
10.1103/PhysRevB.96.241411

Publication date:
2017

Document Version
Publisher's PDF, also known as Version of record

PHYSICAL REVIEW B **96**, 241411(R) (2017)

Symmetry-forbidden intervalley scattering by atomic defects in monolayer transition-metal dichalcogenides

Kristen Kaasbjerg,[1,*] Johannes H. J. Martiny,[1] Tony Low,[2] and Antti-Pekka Jauho[1]

[1]*Center for Nanostructured Graphene (CNG), Department of Micro- and Nanotechnology, Technical University of Denmark, DK-2800 Kongens Lyngby, Denmark*

[2]*Department of Electrical and Computer Engineering, University of Minnesota, Minneapolis, Minnesota 55455, USA*

(Received 29 August 2017; published 21 December 2017)

Intervalley scattering by atomic defects in monolayer transition-metal dichalcogenides (TMDs; MX_2) presents a serious obstacle for applications exploiting their unique valley-contrasting properties. Here, we show that the symmetry of the atomic defects can give rise to an unconventional protection mechanism against intervalley scattering in monolayer TMDs. The predicted defect-dependent selection rules for intervalley scattering can be verified via Fourier transform scanning tunneling spectroscopy (FT-STS), and provide a unique identification of, e.g., atomic vacancy defects (M vs X). Our findings put the absence of the intervalley FT-STS peak in recent experiments in a different perspective.

DOI: 10.1103/PhysRevB.96.241411

Introduction. Two-dimensional (2D) monolayers of transition-metal dichalcogenides (TMDs; MX_2) are promising candidates for spin- and valleytronics applications [1]. Their hallmarks include unique valley-contrasting properties and strong spin-valley coupling [1,2] exemplified by, e.g., valley-selective optical pumping [3–5], a valley-dependent Zeeman effect [6–9], and the valley Hall effect [10]. Such means to control the valley degree of freedom are instrumental for valleytronics applications.

Another prerequisite for a successful realization of valleytronics is a sufficiently long valley lifetime [11,12]; atomic defects are a common limiting factor which can provide the required momentum for intervalley scattering due to their short-range nature. However, as illustrated in Fig. 1(a), the spin-orbit (SO)-induced spin-valley coupling in the K, K' valleys of 2D TMDs partially protects the valley degree of freedom against relaxation via intervalley scattering by nonmagnetic defects [2]. Due to the small spin-orbit splitting in the conduction-band valleys [13,14], only the valence-band valleys fully benefit from this protection. Identification of additional protection mechanisms in the conduction band would hence be advantageous for valleytronics in 2D TMDs.

In this Rapid Communication, we demonstrate that besides the spin-valley coupling, the symmetry and position of atomic defects give rise to unconventional selection rules for intervalley quasiparticle scattering in 2D TMDs. As illustrated in Fig. 1(b), we find that for defects with threefold rotational symmetry (C_3), e.g., atomic vacancies, intervalley $K \leftrightarrow K'$ scattering in the conduction band is forbidden for defects centered on the X site while it is allowed for M centered defects. In the valence band, intervalley scattering is forbidden in both cases. Analogous selection rules for the intervalley coupling due to confinement potentials in 2D TMD-based quantum dots have previously been noted [15].

Our findings can be readily verified with scanning tunneling spectroscopy (STS) which has provided valuable insight to the electronic properties of 2D TMDs [16–20]. In particular, Fourier transform STS (FT-STS) is a powerful method for investigating atomic defects and their scattering properties in 2D materials [21,22]. The measured STS map is a probe of the local density of states (LDOS) whose real-space modulation, resembling Friedel oscillations, originates from quasiparticle interference (QPI) between electronic waves scattered by defects. Hence, the Fourier transform of the STS map provides direct access to the available scattering channels in $\mathbf{q}$ space, and has shed important light on defect scattering in, e.g., graphene [23–30], monolayer TMDs [18,19], and black phosphorus [31].

In the above-mentioned STS experiments on TMDs, the strong spin-valley coupling in the valence band of WSe_2 was confirmed by the missing $K \leftrightarrow K'$ intervalley peak in the FT-STS spectrum [18,19]. Surprisingly, the intervalley peak was also missing in the conduction band where intervalley scattering should be allowed [18,19] [see Fig. 1(a)].

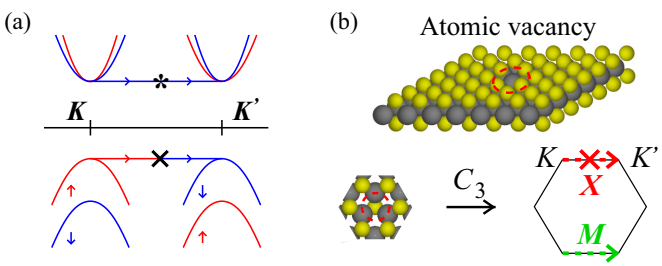

FIG. 1. Symmetry-dependent defect scattering in monolayer TMDs. (a) Sketch of the band structure near the K, K' points. The strong spin-valley coupling in the valence band suppresses intervalley scattering (×). In the conduction band, the small spin-orbit splitting, in principle, allows for intervalley scattering (∗). However, for defects with threefold rotational symmetry (C_3), additional selection rules arise which protect against intervalley scattering. (b) Atomic sulfur vacancy in 2D MoS_2 showing the C_3 symmetry of the vacancy site. The vacancy-dependent selection rules for $K \leftrightarrow K'$ intervalley scattering in the conduction band are illustrated in the bottom part, showing that only M vacancies produce intervalley scattering (green arrow). This allows for a unique identification of the vacancy type with FT-STS.

*kkaa@nanotech.dtu.dk

Here, we demonstrate the effect of symmetry on quasiparticle scattering by atomic vacancies which are among the most common types of defects in 2D TMDs [32–38]. For this purpose, we perform atomistic density-functional (DFT)-based T-matrix calculations [39] of FT-STS and QPI spectra for vacancies in two archetypal TMDs: the direct gap [44], small SO split MoS_2, and the indirect gap [17], large SO split [13,14] WSe_2. As we show, the $K \leftrightarrow K'$ conduction-band intervalley FT-STS peak is strongly suppressed for X vacancies while it appears clearly for M vacancies, thus offering an appealing explanation for its conspicuous absence in experiments [18,19]. Our findings furthermore show that FT-STS allows for a unique identification of the vacancy type, and indicate that the valley dynamics of carriers and excitons in 2D TMDs are not affected by disorder if M-type defects can be avoided.

Symmetry-dependent intervalley scattering. We consider first the effect of symmetry on intervalley scattering by defects in 2D TMDs. The selection rules can be deduced within the framework of the low-energy Hamiltonian [2],

$$\mathcal{H}(\mathbf{k}) = at(\tau k_x \hat{\sigma}_x + k_y \hat{\sigma}_y) + \frac{\Delta}{2}\hat{\sigma}_z + \tau\lambda\frac{\hat{1}-\hat{\sigma}_z}{2}\hat{s}_z, \qquad (1)$$

describing the band structure in the K,K' valleys sketched in Fig. 1(a). Here, a is the lattice constant, t is a hopping parameter, $\tau = \pm 1$ is the K,K' valley index, Δ is the band gap, 2λ is the SO splitting at the top of the valence band, and $\hat{\sigma}$, $\hat{\tau}$, and $\hat{s}$ are Pauli matrices in the symmetry-adapted spinor basis, valley, and spin space, respectively. The symmetry-adapted basis is spanned by the M d orbitals $|\phi_{v\tau}\rangle = 1/\sqrt{2}(|d_{x^2-y^2}\rangle + i\tau|d_{xy}\rangle)$ and $|\phi_{c\tau}\rangle = |d_{z^2}\rangle$ which dominate the states in the valence (v) and conduction (c) bands, respectively [45,46].

In 2D TMDs, defects such as atomic vacancies have C_3 symmetry, i.e., $\hat{V}_i = C_3\hat{V}_i C_3^\dagger$, where $\hat{V}_i$ is the scattering potential for defect type i and C_3 is the operator for threefold rotations by $\pm 2\pi/3$ around the defect center. The intervalley matrix element ($\tau \neq \tau'$) between the high-symmetry K,K' points can thus be written

$$\begin{aligned}\langle n\tau|\hat{V}_i|n\tau'\rangle &= \langle n\tau|C_3^\dagger C_3\hat{V}_i C_3^\dagger C_3|n\tau'\rangle \\ &= \langle n\tau|C_3^\dagger\hat{V}_i C_3|n\tau'\rangle \equiv \gamma_{i,n}^{\tau\tau'}\langle n\tau|\hat{V}_i|n\tau'\rangle, \qquad (2)\end{aligned}$$

where n is the band index (including spin) and $\hat{I} = C_3^\dagger C_3$ is the identity operator. As C_3 belongs to the group of the wave vector at the K,K' points (C_{3h}), the Bloch functions transform according to the irreducible representation of C_{3h}, $C_3|n\tau\rangle = w_{i,n\tau}|n\tau\rangle$, where $w_{i,n\tau}$ denotes the eigenvalues of C_3. The matrix element can thus be expressed in terms of the complex scalar $\gamma_{i,n}^{\tau\tau'} = w_{i,n\tau}^* w_{i,n\tau'}$, as indicated in the last equality of (2). Our analysis shows that $\gamma_{i,n}^{\tau\tau'} = 1$ only if the defect is centered on an M site and $n = c$ [39]. In all other cases, $\gamma_{i,n}^{\tau\tau'} \neq 1$, and the intervalley matrix element vanishes identically by virtue of Eq. (2).

The symmetry argument is completely general, and thus applies to all types of M,X-centered defects in 2D TMDs with C_3 symmetry, e.g., complex defect structures [32,36], adatoms, and substitutional atoms [37]. As Eq. (1) is diagonal in spin space, it furthermore holds for intervalley spin-flip scattering by magnetic defects.

FT-STS theory. Next, we outline a general T-matrix-based Green's function approach for the calculation of the FT-STS spectra. In STS, the measured real-space QPI pattern is related to the differential conductance $dI/dV \propto \rho(\mathbf{r},\varepsilon)$ [47], and hence the LDOS $\rho(\mathbf{r},\varepsilon) = -1/\pi\,\mathrm{Im}[G(\mathbf{r},\mathbf{r};\varepsilon)]$, where $G(\mathbf{r},\mathbf{r}';\varepsilon) = \langle\mathbf{r}|\hat{G}(\varepsilon)|\mathbf{r}'\rangle$ is the Green's function (GF) in real space in the presence of a defect. Expressing the GF in a basis of Bloch states $\psi_{n\mathbf{k}}(\mathbf{r})$, $G(\mathbf{r},\mathbf{r}';\varepsilon) = \sum_{mn}\sum_{\mathbf{k}\mathbf{k}'}\psi_{nk'}^*(\mathbf{r})\psi_{m\mathbf{k}}(\mathbf{r}')G_{\mathbf{k}\mathbf{k}'}^{mn}(\varepsilon)$, where $\mathbf{k}$ is the wave vector and m,n band indices, the FT-STS spectrum given by the 2D Fourier transform of $\rho(\mathbf{r},\varepsilon)$ can be obtained as [39]

$$\begin{aligned}\rho(\mathbf{q}+\mathbf{G},\varepsilon) &= \int d\mathbf{r}\, e^{-i(\mathbf{q}+\mathbf{G})\cdot\mathbf{r}_\parallel}\rho(\mathbf{r},\varepsilon) \\ &= \frac{1}{2\pi i}\sum_{mn,\mathbf{k}} n_{\mathbf{k},\mathbf{q}}^{mn}(\mathbf{G})\left[G_{\mathbf{k},\mathbf{k}+\mathbf{q}}^{mn}(\varepsilon)^* - G_{\mathbf{k}+\mathbf{q},\mathbf{k}}^{nm}(\varepsilon)\right], \qquad (3)\end{aligned}$$

where $\mathbf{r} = (\mathbf{r}_\parallel, z)$, $\mathbf{k},\mathbf{q} \in$ 1st Brillouin zone (BZ), $\mathbf{G}$ is a reciprocal lattice vector, and $G_{\mathbf{k}\mathbf{k}'}^{mn}(\varepsilon) = \langle\psi_{m\mathbf{k}}|\hat{G}(\varepsilon)|\psi_{n\mathbf{k}'}\rangle$ is the Bloch function representation of the GF. The matrix element $n_{\mathbf{k},\mathbf{q}}^{mn}(\mathbf{G}) = \langle\psi_{m\mathbf{k}}|e^{-i(\mathbf{q}+\mathbf{G})\cdot\hat{\mathbf{r}}_\parallel}|\psi_{n\mathbf{k}+\mathbf{q}}\rangle$ is important in many aspects. For example, it describes the FT-STS Bragg peaks ($\mathbf{G} \neq \mathbf{0}$), and hence the atomic modulation of the LDOS inside the unit cell. It also plays a central role in systems with (pseudo)spin texture, e.g., graphene and spin-orbit materials, as it contains the spinor overlap [48]. This is less important in 2D TMDs where the eigenstates of Eq. (1) are characterized by predominantly polarized spinor states [49] with trivial pseudospin $\hat{\sigma}$ and spin $\hat{s}$ textures.

For a single defect, the *exact* GF taking into account multiple scattering off the defect is given by the T matrix as

$$\mathbf{G}_{\mathbf{k}\mathbf{k}'}(\varepsilon) = \delta_{\mathbf{k},\mathbf{k}'}\mathbf{G}_{\mathbf{k}}^0(\varepsilon) + \mathbf{G}_{\mathbf{k}}^0(\varepsilon)\mathbf{T}_{\mathbf{k}\mathbf{k}'}(\varepsilon)\mathbf{G}_{\mathbf{k}'}^0(\varepsilon), \qquad (4)$$

where the boldface symbols denote matrices in band and spin indices, and the diagonal *bare* GF is given by the band energies, $G_{n\mathbf{k}}^0(\varepsilon) = (\varepsilon - \varepsilon_{n\mathbf{k}} + i\eta)^{-1}$. The last term in Eq. (4) comprises the nondiagonal, defect-induced correction $\delta\mathbf{G}_{\mathbf{k},\mathbf{k}+\mathbf{q}}$ to the GF. To isolate the FT-STS features related to the defect, we substitute $G \to \delta G$ in Eq. (3) in our FT-STS calculations.

The T matrix obeys the integral equation

$$\mathbf{T}_{\mathbf{k}\mathbf{k}'}(\varepsilon) = \mathbf{V}_{\mathbf{k}\mathbf{k}'}^i + \sum_{\mathbf{k}''}\mathbf{V}_{\mathbf{k}\mathbf{k}''}^i\mathbf{G}_{\mathbf{k}''}^0(\varepsilon)\mathbf{T}_{\mathbf{k}''\mathbf{k}'}(\varepsilon), \qquad (5)$$

where $V_{i,\mathbf{k}\mathbf{k}'}^{mn}$ are matrix elements of the defect potential and the second term describes virtual transitions to intermediate states with wave vector $\mathbf{k}''$.

For nonmagnetic defects, we take $\hat{V}_i = V_i(\hat{\mathbf{r}}) \otimes \hat{s}_0$, where $\hat{s}_0$ is the identity operator in spin space. With the spin indices written out explicitly, the defect matrix elements can be expressed as

$$\begin{aligned}V_{i,\mathbf{k}\mathbf{k}'}^{mn}(s,s') &= \langle m\mathbf{k}s|\hat{V}_i|n\mathbf{k}'s'\rangle \\ &= \sum_{s_z}\langle m\mathbf{k}s;s_z|V_i(\hat{\mathbf{r}})|n\mathbf{k}'s';s_z\rangle, \qquad (6)\end{aligned}$$

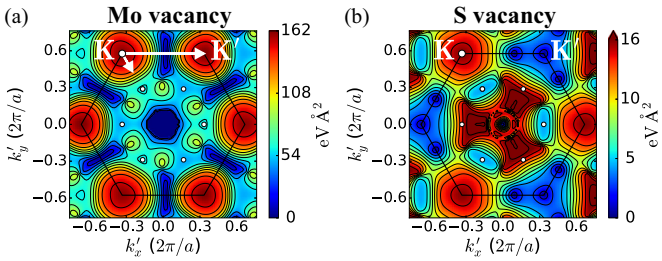

FIG. 2. Defect matrix elements for the conduction band in 2D MoS_2 calculated with our DFT-based supercell method. The plots show $|V^{cc}_{i,\mathbf{kk}'}(s,s)|$ for (a) a Mo, and (b) a S vacancy as a function of $\mathbf{k}'$ with the initial state fixed to $\mathbf{k}=\mathbf{K}$. Note the different disorder strengths (colorbar scales) for the two types of vacancies as well as the vanishing intervalley matrix element [long arrow in (a)] for S vacancies.

with $|\cdot;s_z\rangle$ denoting the $s_z=\pm1$ spinor component of the wave function. Here, we use a DFT method based on an atomic supercell model for the defect site illustrated in Fig. 1(b) to calculate the defect matrix elements [39].

As an example, Fig. 2 shows the spin-diagonal conduction-band matrix elements for Mo and S vacancies in 2D MoS_2. While the Mo vacancy gives rise to intravalley (short arrow) and intervalley (long arrow) couplings, the intervalley matrix element for the S vacancy vanishes, thus confirming the symmetry-based predictions in Eq. (2). Furthermore, we note that the matrix element in the K,K' valleys is an order of magnitude larger for Mo than for S vacancies. In a simple picture where only K,K' intra- and intervalley scattering with a constant matrix element V_0 is considered, the T matrix becomes $T(\varepsilon)=V_0/[1-gV_0\bar{G}_0(\varepsilon)]$, where $\bar{G}_0(\varepsilon)=\int\frac{d\mathbf{k}}{(2\pi)^2}G^0_{c\mathbf{k}}(\varepsilon)\propto\rho_c$, $\rho_c\approx0.01$ eV^{-1} Å^{-2} is the density of states, and the valley multiplication factor $g=2$ (=1) for M (X; only intravalley scattering) vacancies. Together with the values for V_0 extracted from Fig. 2, this allows us to identify M ($g\rho_cV_0>1$) and X ($g\rho_cV_0<1$) vacancies as *strong* (unitary), $T(\varepsilon)\approx-1/g\bar{G}_0(\varepsilon)$, and *weak*, $T(\varepsilon)\approx V_0$, defects, respectively.

The FT-STS calculations presented below are based on full BZ $\mathbf{k},\mathbf{q}$-point samplings of the band structures, defect matrix elements, and $n^{mn}_{\mathbf{k},\mathbf{q}}(\mathbf{G})$ matrix elements, all obtained with DFT-LDA including a SO interaction [39]. Our approach naturally goes beyond the low-energy description in Eq. (1), which is essential as both the K and Q valleys are relevant for quasiparticle scattering in 2D TMDs. As intervalley scattering in the valence band is suppressed by (i) the large spin-valley coupling, and (ii) the C_3 symmetry of the vacancies, the valence-band FT-STS spectra are rather simple [18,19], and we here limit the discussion to the conduction band. We furthermore focus on features related to the symmetry-forbidden intervalley scattering, deferring a complete analysis to a forthcoming paper.

FT-STS and QPI spectra. The calculated band structures and FT-STS spectra for atomic vacancies in MoS_2 and WSe_2 are summarized in Fig. 3. The different conduction-band structures in the two materials (K vs Q valley alignment and magnitude of the SO splitting), shown in the insets in Fig. 3(a), and the vacancy-dependent intervalley matrix element result in markedly different spectra between the materials as well as the vacancy type.

In general, the FT-STS spectra close to the band edge ($\varepsilon\approx0$; see Ref. [39]) are characterized by featureless spots at the points in $\mathbf{q}$ space corresponding to intravalley ($\mathbf{q}=\mathbf{0}$) and intervalley scattering [$\mathbf{q}_{1\text{–}5}$ in Fig. 3(b)]. The spot intensities

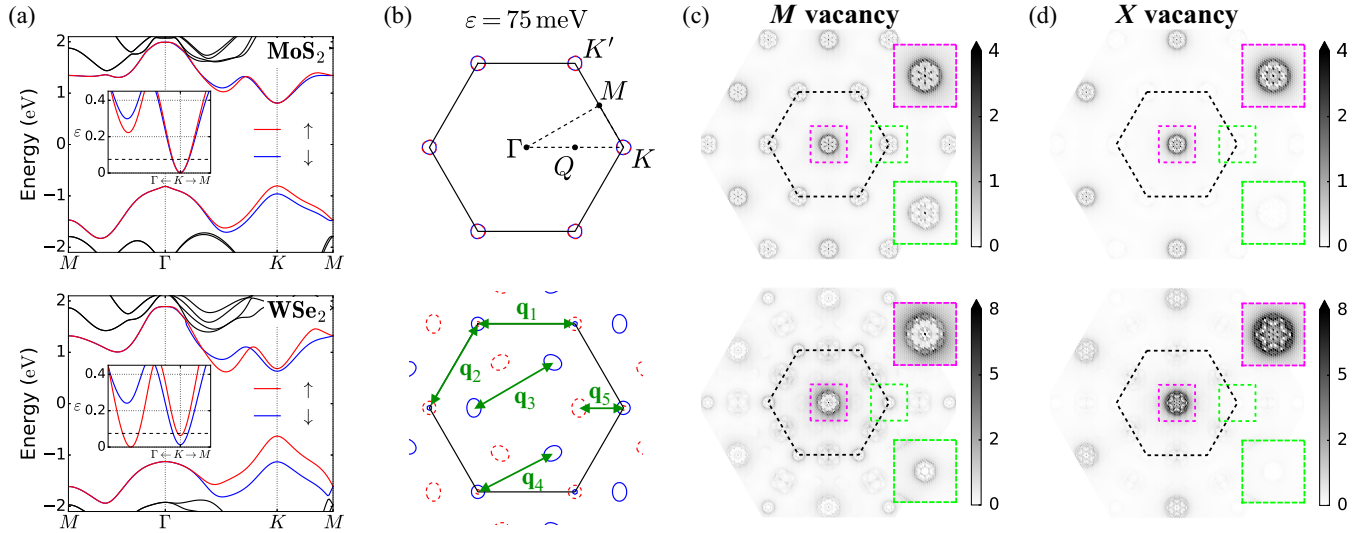

FIG. 3. Band structures and FT-STS spectra for atomic vacancies in MoS_2 (top) and WSe_2 (bottom). (a) Band structures including SO interaction. The insets show a zoom of the SO split conduction-band K,Q valleys with the energy $\varepsilon=E-E_c$ measured relative to the band edge E_c. The dashed lines indicate the energy of the constant-energy surfaces in (b) and the FT-STS spectra in (c), (d). (b) Constant-energy surfaces in $\mathbf{k}$ space for $\varepsilon=75$ meV, together with high-symmetry $\mathbf{k}$ points in the Brillouin zone (top) and representative intervalley $\mathbf{q}$ vectors (bottom). (c), (d) FT-STS spectra at $\varepsilon=75$ meV for (c) $M=$ Mo,W and (d) $X=$ S, Se vacancies. The boxes show zooms of the marked regions.

are governed by the T-matrix scattering amplitude and valley degeneracy. For the Bragg peaks, the intensity is reduced compared to those in the first BZ due to the phase-factor matrix element $n^{mn}_{\mathbf{k},\mathbf{q}}(\mathbf{G})$.

In MoS_2 the SO splitting in the conduction band is small, ∼3 meV, thereby allowing for spin-conserving $K \leftrightarrow K'$ intervalley scattering ($\mathbf{q}_{1,2}$) near the band edge. Hence, intervalley peaks at $\mathbf{q} = \mathbf{K},\mathbf{K}'$ are to be expected. In WSe_2 the Q valley is lower than the K valley and the SO splitting is much larger (∼250 meV in the Q valley and ∼50 meV the K valley), hence a $\mathbf{q} \approx \mathbf{M}$ peak due to $Q \leftrightarrow Q'$ intervalley processes ($\mathbf{q}_3$) will appear instead.

The above is indeed the case in the FT-STS spectra for M vacancies shown in Fig. 3(c) for an energy $\varepsilon = 75$ meV above the band edge [dashed lines in the insets in Fig. 3(a)]. At this energy, the spots have developed into features (see the zoomed insets) which are dominated by processes involving nesting vectors between parallel segments of the constant energy contour being probed. In MoS_2 with almost isotropic energy contours, $\varepsilon(k) = \varepsilon$, intravalley backscattering with $q = 2k$ therefore produces circular features. Trigonal warping of the constant energy surfaces gives rise to additional approximate nesting vectors which produce starlike patterns with hexagonal symmetry around the Γ point and triangular symmetry near the K,K' points as in graphene [30]. The intervalley features are weaker than the intravalley feature because intravalley processes in the K and K' valleys add up, while the two $K \leftrightarrow K'$ intervalley processes have distinct wave vectors, $\mathbf{q} \approx \pm\mathbf{K}$. In WSe_2, both the Q and K valleys are accessible at $\varepsilon = 75$ meV, and therefore intervalley features around $\mathbf{q} \approx \mathbf{M}$, $\mathbf{q} \approx \mathbf{K}$, as well as $\mathbf{q} \approx \mathbf{Q}$ are observed. They are associated with $Q \leftrightarrow Q/K \leftrightarrow Q$ ($\mathbf{q}_{3/4}$), $K \leftrightarrow K'$ ($\mathbf{q}_{1,2}$), and $K \leftrightarrow Q$ ($\mathbf{q}_5$) processes, respectively. The central intravalley feature in WSe_2 has more structure than in MoS_2 as it has contributions from both K and Q intravalley processes. At even higher energies (not shown), the K and Q valleys are available in both MoS_2 and WSe_2, and the FT-STS spectra become highly complex.

In contrast to the FT-STS spectra for M vacancies, the spectra for X vacancies in Fig. 3(d) show that the anticipated intervalley feature at $\mathbf{q} \approx \mathbf{K}$ ($\mathbf{q}_{1,2}$) is strongly suppressed for both MoS_2 and WSe_2. This is a direct consequence of the symmetry-forbidden $K \leftrightarrow K'$ intervalley matrix element which suppresses intervalley scattering also in the vicinity of the high-symmetry K,K' points [see Fig. 2(b)]. In WSe_2, also the $Q \leftrightarrow Q'$ ($\mathbf{q}_3$) and $Q \leftrightarrow K$ ($\mathbf{q}_{4,5}$) intervalley features are much weaker for X vacancies, which can be traced back to overall small intervalley matrix elements.

The suppression of $K \leftrightarrow K'$ intervalley scattering for X vacancies leaves a clear fingerprint in the real-space LDOS, as demonstrated by the QPI maps in Fig. 4 for Mo and S vacancies in MoS_2. They have been obtained by Fourier transforming the FT-STS spectra in Figs. 3(c) and 3(d), $\rho(\mathbf{r}_\parallel,\varepsilon) = \sum_{\mathbf{G}} \int \frac{d\mathbf{q}}{(2\pi)^2} e^{i(\mathbf{q}+\mathbf{G})\cdot\mathbf{r}_\parallel} \rho(\mathbf{q}+\mathbf{G},\varepsilon)$. For both vacancies, the LDOS modulation has a threefold symmetry and decays away the vacancy site (marked by crosses). The observed atomic resolution can be attributed to the FT-STS Bragg peaks, and shows that the LDOS modulation is concentrated on the Mo sites of the lattice, in accordance with the Mo

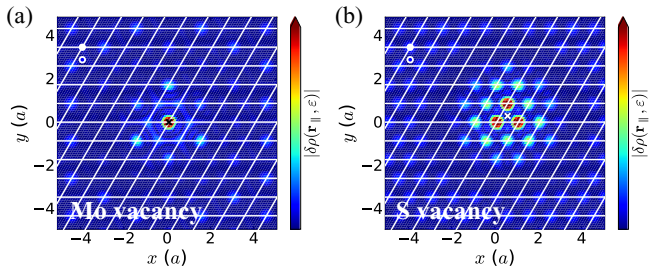

FIG. 4. Real-space QPI maps for 2D MoS_2 showing the defect-induced change in the LDOS $\delta\rho(\mathbf{r}_\parallel,\varepsilon)$ around (a) a Mo, and (b) a S vacancy. The lines show the unit cells of the lattice with lattice constant a, and the atomic positions inside the unit cell and the position of the vacancy are indicated by the symbols (solid circle: Mo; open circle: S; cross: vacancy).

d-orbital character of the conduction-band states in the K,K' valleys [cf. Eq. (1)]. Noticeably, the QPI map for the S vacancy stands out by the absence of an intervalley-scattering-induced cell-to-cell modulation of the LDOS in the vicinity of the vacancy, which is clearly visible for the Mo vacancy. At larger distances from the vacancy site, a slower modulation with wavelength $2\pi/q$ (≈$10a$ at $\varepsilon = 75$ meV) due to intravalley backscattering, $q = 2k$, emerges.

Conclusions and outlook. In conclusion, we have demonstrated (i) an unconventional symmetry-induced protection against intervalley scattering by atomic defects in 2D TMDs, and (ii) its fingerprint in conduction-band FT-STS spectra which allows for a unique identification of, e.g., the vacancy type. Our findings may offer an explanation why the $K \leftrightarrow K'$ intervalley FT-STS peak has not been observed in experiments [18,19], and are also relevant for FT-STS on metallic TMDs [50].

We are convinced that our work, in conjunction with further experimental FT-STS studies, can provide a complete understanding of defect scattering in 2D TMDs. In addition, FT-STS may shed important light on band-structure issues in 2D TMDs, such as the magnitude of SO splittings [18], the K,Q-valley ordering in the conduction band which is sensitive to the SO strength [13,14], and the subband structure and valley ordering in few-layer TMDs [51,52]. Besides our reported FT-STS signatures, the suppression of intervalley scattering is expected to have implications for a wide range of effects in disordered 2D TMDs, e.g., the optical conductivity [53], magnetotransport [54–58], the valley Hall effect [59], Elliot-Yafet spin relaxation [60], and disorder-induced valley pumping [61].

Acknowledgments. We would like to thank an anonymous reviewer on a related work [62] for suggesting we investigate observable implications of our symmetry finding for intervalley scattering. K.K. acknowledges support from the European Union's Horizon 2020 research and innovation programme under the Marie Sklodowska-Curie Grant Agreement No. 713683 (COFUNDfellowsDTU). T.L. acknowledges support from the National Science Foundation under Grant No. NSF/EFRI-1741660. The Center for Nanostructured Graphene (CNG) is sponsored by the Danish National Research Foundation, Project No. DNRF103.

[1] X. Xu W. Yao, D. Xiao, and T. F. Heinz, Spin and pseudospins in layered transition metal dichalcogenides, Nat. Phys. **10**, 343 (2014).

[2] D. Xiao, G.-B. Liu, W. Feng, X. Xu, and W. Yao, Coupled Spin and Valley Physics in Monolayers of MoS_2 and other Group-VI Dichalcogenides, Phys. Rev. Lett. **108**, 196802 (2012).

[3] K. F. Mak, K. He, J. Shan, and T. F. Heinz, Control of valley polarization in monolayer MoS_2 by optical helicity, Nat. Nanotechnol. **7**, 494 (2012).

[4] H. Zeng, J. Dai, W. Yao, D. Xiao, and X. Cui, Valley polarization in MoS_2 monolayers by optical pumping, Nat. Nanotechnol. **7**, 490 (2012).

[5] T. Cao, G. Wang, W. Han, H. Ye, C. Zhu, J. Shi, Q. Niu, P. Tan, E. Wang, B. Liu, and J. Feng, Valley-selective circular dichroism of monolayer molybdenum disulphide, Nat. Commun. **3**, 887 (2012).

[6] A. Srivastava, M. Sidler, A. V. Allain, D. S. Lembke, A. Kis, and A. Imamoğlu, Valley Zeeman effect in elementary optical excitations of monolayer WSe_2, Nat. Phys. **11**, 141 (2014).

[7] G. Aivazian, Z. Gong, A. M. Jones, R.-L. Chu, J. Yan, D. G. Mandrus, C. Zhang, D. Cobden, W. Yao, and X. Xu, Magnetic control of valley pseudospin in monolayer WSe_2, Nat. Phys. **11**, 148 (2014).

[8] Y. Li, J. Ludwig, T. Low, A. Chernikov, X. Cui, G. Arefe, Y. D. Kim, A. M. van der Zande, A. Rigosi, H. M. Hill, S. H. Kim, J. Hone, Z. Li, D. Smirnov, and T. F. Heinz, Valley Splitting and Polarization by the Zeeman Effect in Monolayer $MoSe_2$, Phys. Rev. Lett. **113**, 266804 (2014).

[9] D. MacNeill, C. Heikes, K. F. Mak, Z. Anderson, A. Kormányos, V. Zólyomi, J. Park, and D. C. Ralph, Breaking of Valley Degeneracy by Magnetic Field in Monolayer $MoSe_2$, Phys. Rev. Lett. **114**, 037401 (2015).

[10] K. F. Mak, K. L. McGill, J. Park, and P. L. McEuen, The valley Hall effect in MoS_2 transistors, Science **344**, 1489 (2014).

[11] L. Yang, N. A. Sinitsyn, W. Chen, J. Yuan, J. Zhang, J. Lou, and S. A. Crooker, Long-lived nanosecond spin relaxation and spin coherence of electrons in monolayer MoS_2 and WS_2, Nat. Phys. **11**, 830 (2015).

[12] T. Yan, S. Yang, D. Li, and X. Cui, Long valley relaxation time of free carriers in monolayer WSe_2, Phys. Rev. B **95**, 241406(R) (2017).

[13] Z. Y. Zhu, Y. C. Cheng, and U. Schwingenschlögl, Giant spin-orbit-induced spin splitting in two-dimensional transition-metal dichalcogenide semiconductors, Phys. Rev. B **84**, 153402 (2011).

[14] K. Kośmider, J. W. González, and J. Fernández-Rossier, Large spin splitting in the conduction band of transition metal dichalcogenide monolayers, Phys. Rev. B **88**, 245436 (2013).

[15] G.-B. Liu, H. Pang, Y. Yao, and W. Yao, Intervalley coupling by quantum dot confinement potentials in monolayer transition metal dichalcogenides, New J. Phys. **16**, 105011 (2014).

[16] C.-P. Lu, G. Li, J. Mao, L.-M. Wang, and E. Y. Andrei, Bandgap, mid-gap states, and gating effects in MoS_2, Nano Lett. **14**, 4628 (2014).

[17] C. Zhang, Y. Chen, A. Johnson, M.-Y. Li, L.-J. Li, P. C. Mendell, R. M. Feenstra, and C.-K. Shih, Probing critical point energies of transition metal dichalcogenides: Surprising indirect gap of single layer WSe_2, Nano Lett. **15**, 6494 (2015).

[18] H. Liu, J. Chen, H. Yu, F. Yang, L. Jiao, G.-B. Liu, W. Ho, C. Gao, J. Jia, W. Yao, and M. Xie, Observation of intervalley quantum interference in epitaxial monolayer tungsten diselenide, Nat. Commun. **6**, 8180 (2015).

[19] M. Yankowitz, D. McKenzie, and B. J. LeRoy, Local Spectroscopic Characterization of Spin and Layer Polarization in WSe_2, Phys. Rev. Lett. **115**, 136803 (2015).

[20] X. Zhou, K. Kang, S. Xie, A. Dadgar, N. R. Monahan, X.-Y. Zhu, J. Park, and A. N. Pasupathy, Atomic-scale spectroscopy of gated monolayer MoS_2, Nano Lett. **16**, 3148 (2016).

[21] L. Simon, C. Bena, F. Vonau, M. Cranney, and D. Aubel, Fourier-transform scanning tunneling spectroscopy: The possibility to obtain constant-energy maps and band dispersion using a local measurement, J. Phys. D **44**, 464010 (2011).

[22] L. Chen, P. Cheng, and K. Wu, Quasiparticle interference in unconventional 2D systems, J. Phys.: Condens. Matter **29**, 103001 (2017).

[23] G. M. Rutter, J. N. Crain, N. P. Guisinger, T. Li, P. N. First, and J. A. Stroscio, Scattering and interference in epitaxial graphene, Science **317**, 219 (2007).

[24] P. Mallet, F. Varchon, C. Naud, L. Magaud, C. Berger, and J.-Y. Veuillen, Electron states of mono- and bilayer graphene on SiC probed by scanning-tunneling microscopy, Phys. Rev. B **76**, 041403(R) (2007).

[25] C. Bena, Effect of a Single Localized Impurity on the Local Density of States in Monolayer and Bilayer Graphene, Phys. Rev. Lett. **100**, 076601 (2008).

[26] I. Brihuega, P. Mallet, C. Bena, S. Bose, C. Michaelis, L. Vitali, F. Varchon, L. Magaud, K. Kern, and J.-Y. Veuillen, Quasiparticle Chirality in Epitaxial Graphene Probed at the Nanometer Scale, Phys. Rev. Lett. **101**, 206802 (2008).

[27] T. Pereg-Barnea and A. H. MacDonald, Chiral quasiparticle local density of states maps in graphene, Phys. Rev. B **78**, 014201 (2008).

[28] P. Mallet, I. Brihuega, S. Bose, M. M. Ugeda, J. M. Gómez-Rodríguez, K. Kern, and J.-Y. Veuillen, Role of pseudospin in quasiparticle interferences in epitaxial graphene probed by high-resolution scanning tunneling microscopy, Phys. Rev. B **86**, 045444 (2012).

[29] M. Settnes, S. R. Power, D. H. Petersen, and A.-P. Jauho, Theoretical Analysis of a Dual-Probe Scanning Tunneling Microscope Setup on Graphene, Phys. Rev. Lett. **112**, 096801 (2014).

[30] D. Dombrowski, W. Jolie, M. Petrović, S. Runte, F. Craes, J. Klinkhammer, M. Kralj, P. Lazić, E. Sela, and C. Busse, Energy-Dependent Chirality Effects in Quasifree-Standing Graphene, Phys. Rev. Lett. **118**, 116401 (2017).

[31] B. Kiraly, N. Hauptmann, A. N. Rudenko, M. I. Katsnelson, and A. A. Khajetoorians, Probing single vacancies in black phosphorus at the atomic level, Nano Lett. **17**, 3607 (2017).

[32] W. Zhou, X. Zou, S. Najmaei, Z. Liu, Y. Shi, J. Kong, J. Lou, P. M. Ajayan, B. I. Yakobson, and J.-C. Idrobo, Intrinsic structural defects in monolayer molybdenum disulfide, Nano Lett. **13**, 2615 (2013).

[33] B. W. H. Baugher, H. O. H. Churchill, Y. Yang, and P. Jarillo-Herrero, Intrinsic electronic transport properties of high-quality monolayer and bilayer MoS_2, Nano Lett. **13**, 4212 (2013).

[34] H. Schmidt, S. Wang, L. Chu, M. Toh, R. Kumar, W. Zhao, A. H. C. Neto, J. Martin, S. Adam, B. Özyilmaz, and G. Eda, Transport properties of monolayer MoS_2 grown by chemical vapor deposition, Nano Lett. **14**, 1909 (2014).

[35] Z. Yu, Y. Pan, Y. Shen, Z. Wang, Z.-Y. Ong, T. Xu, R. Xin, L. Pan, B. Wang, L. Sun, J. Wang, G. Zhang, Y. W. Zhang, Y. Shi, and X. Wang, Towards intrinsic charge transport in monolayer molybdenum disulfide by defect and interface engineering, Nat. Commun. **5**, 5290 (2014).

[36] Y.-C. Lin, T. Björkman, H.-P. Komsa, P.-Y. Teng, C.-H. Yeh, F.-S. Huang, K.-H. Lin, J. Jadczak, Y.-S. Huang, P.-W. Chiu, A. V. Krasheninnikov, and K. Suenaga, Three-fold rotational defects in two-dimensional transition metal dichalcogenides, Nat. Commun. **6**, 6736 (2014).

[37] J. Hong, Z. Hu, M. Probert, K. Li, D. Lv, X. Yang, L. Gu, N. Mao, Q. Feng, L. Xie, J. Zhang, D. Wu, Z. Zhang, C. Jin, W. Ji, X. Zhang, J. Yuan, and Z. Zhang, Exploring atomic defects in molybdenum disulphide monolayers, Nat. Commun. **6**, 6293 (2015).

[38] S. Zhang, C.-G. Wang, M.-Y. Li, D. Huang, L.-J. Li, W. Ji, and S. Wu, Defect Structure of Localized Excitons in a WSe_2 Monolayer, Phys. Rev. Lett. **119**, 046101 (2017).

[39] See Supplemental Material at http://link.aps.org/supplemental/10.1103/PhysRevB.96.241411 for details on (i) the derivation of Eq. (3), (ii) the DFT-based calculations of the FT-STS spectra and the involved quantities, (iii) additional FT-STS spectra at the band edge, and (iv) the symmetry analysis of the defect matrix elements, which includes Refs. [40–43].

[40] J. J. Mortensen, L. B. Hansen, and K. W. Jacobsen, Real-space grid implementation of the projector augmented wave method, Phys. Rev. B **71**, 035109 (2005).

[41] A. H. Larsen, M. Vanin, J. J. Mortensen, K. S. Thygesen, and K. W. Jacobsen, Localized atomic basis set in the projector augmented wave method, Phys. Rev. B **80**, 195112 (2009).

[42] J. Enkovaara *et al.*, Electronic structure calculations with GPAW: A real-space implementation of the projector augmented-wave method, J. Phys.: Condens. Matter **22**, 253202 (2010).

[43] T. Olsen, Designing in-plane heterostructures of quantum spin Hall insulators from first principles: $1T'$-MoS_2 with adsorbates, Phys. Rev. B **94**, 235106 (2016).

[44] K. F. Mak, C. Lee, J. Hone, J. Shan, and T. F. Heinz, Atomically Thin MoS_2: A New Direct-Gap Semiconductor, Phys. Rev. Lett. **105**, 136805 (2010).

[45] E. Cappelluti, R. Roldán, J. A. Silva-Guillén, P. Ordejón, and F. Guinea, Tight-binding model and direct-gap/indirect-gap transition in single-layer and multilayer MoS_2, Phys. Rev. B **88**, 075409 (2013).

[46] G.-B. Liu, W.-Y. Shan, Y. Yao, W. Yao, and D. Xiao, Three-band tight-binding model for monolayers of group-VIB transition metal dichalcogenides, Phys. Rev. B **88**, 085433 (2013).

[47] G. A. Fiete and E. J. Heller, *Colloquium*: Theory of quantum corrals and quantum mirages, Rev. Mod. Phys. **75**, 933 (2003).

[48] Y. Kohsaka, T. Machida, K. Iwaya, M. Kanou, T. Hanaguri, and T. Sasagawa, Spin-orbit scattering visualized in quasiparticle interference, Phys. Rev. B **95**, 115307 (2017).

[49] W.-Y. Shan, H.-Z. Lu, and D. Xiao, Spin Hall effect in spin-valley coupled monolayers of transition metal dichalcogenides, Phys. Rev. B **88**, 125301 (2013).

[50] T. Machida, Y. Kohsaka, K. Iwaya, R. Arita, T. Hanaguri, R. Suzuki, M. Ochi, and Y. Iwasa, Orbital-dependent quasiparticle scattering interference in $3R$-NbS_2, Phys. Rev. B **96**, 075206 (2017).

[51] R. Roldán, J. A. Silva-Guillén, M. P. López-Sancho, F. Guinea, E. Cappelluti, and P. Ordejón, Electronic properties of single-layer and multilayer transition metal dichalcogenides MX_2 ($M = \mathrm{Mo,W}$ and $X = \mathrm{S, Se}$), Ann. Phys. **526**, 347 (2014).

[52] A. M. Jones, H. Yu, J. S. Ross, P. Klement, N. J. Ghimire, J. Yan, D. G. Mandrus, W. Yao, and X. Xu, Spin-layer locking effects in optical orientation of exciton spin in bilayer WSe_2, Nat. Phys. **10**, 130 (2014).

[53] S. Yuan, R. Roldán, M. I. Katsnelson, and F. Guinea, Effect of point defects on the optical and transport properties of MoS_2 and WS_2, Phys. Rev. B **90**, 041402(R) (2014).

[54] H.-Z. Lu, W. Yao, D. Xiao, and S.-Q. Shen, Intervalley Scattering and Localization Behaviors of Spin-Valley Coupled Dirac Fermions, Phys. Rev. Lett. **110**, 016806 (2013).

[55] H. Ochoa, F. Finocchiaro, F. Guinea, and V. I. Fal'ko, Spin-valley relaxation and quantum transport regimes in two-dimensional transition-metal dichalcogenides, Phys. Rev. B **90**, 235429 (2014).

[56] A. Kormányos, P. Rakyta, and G. Burkard, Landau levels and Shubnikov–de Haas oscillations in monolayer transition metal dichalcogenide semiconductors, New J. Phys. **17**, 103006 (2015).

[57] H. Schmidt, I. Yudhistira, L. Chu, A. H. C. Neto, B. Özyilmaz, S. Adam, and G. Eda, Quantum Transport and Observation of Dyakonov-Perel Spin-Orbit Scattering in Monolayer MoS_2, Phys. Rev. Lett. **116**, 046803 (2016).

[58] B. Fallahazad, H. C. P. Movva, K. Kim, S. Larentis, T. Taniguchi, K. Watanabe, S. K. Banerjee, and E. Tutuc, Shubnikov–de Haas Oscillations of High Mobility Holes in Monolayer and Bilayer WSe_2: Landau Level Degeneracy, Effective Mass, and Negative Compressibility, Phys. Rev. Lett. **116**, 086601 (2016).

[59] T. Olsen and I. Souza, Valley Hall effect in disordered monolayer MoS_2 from first principles, Phys. Rev. B **92**, 125146 (2015).

[60] H. Ochoa and R. Roldán, Spin-orbit-mediated spin relaxation in monolayer MoS_2, Phys. Rev. B **87**, 245421 (2013).

[61] X.-T. An, J. Xiao, M. W.-Y. Tu, H. Yu, V. I. Fal'ko, and W. Yao, Realization of Valley and Spin Pumps by Scattering at Nonmagnetic Disorders, Phys. Rev. Lett. **118**, 096602 (2017).

[62] K. Kaasbjerg, T. Low, and A.-P. Jauho, Scattering by atomic vacancies in monolayer MoS2: Midgap states, symmetry and screening, arXiv:1612.00469.